Journal Pre-proof

Fabrication of microporous PMMA using ionic liquids: An improved route to classical ScCO$_2$ foaming process

Miriam Trigo-López, S. Vallejos, José A. Reglero Ruiz, Cipriano Ramos, Sagrario Beltrán, Félix C. García, José M. García

Please cite this article as: Trigo-López M, Vallejos S, Reglero Ruiz JoséA, Ramos C, Beltrán S, García FéC, García JoséM, Fabrication of microporous PMMA using ionic liquids: An improved route to classical ScCO$_2$ foaming process, *Polymer* (2019), doi: https://doi.org/10.1016/j.polymer.2019.121867.

This is a PDF file of an article that has undergone enhancements after acceptance, such as the addition of a cover page and metadata, and formatting for readability, but it is not yet the definitive version of record. This version will undergo additional copyediting, typesetting and review before it is published in its final form, but we are providing this version to give early visibility of the article. Please note that, during the production process, errors may be discovered which could affect the content, and all legal disclaimers that apply to the journal pertain.
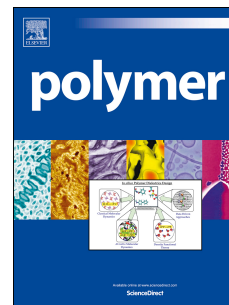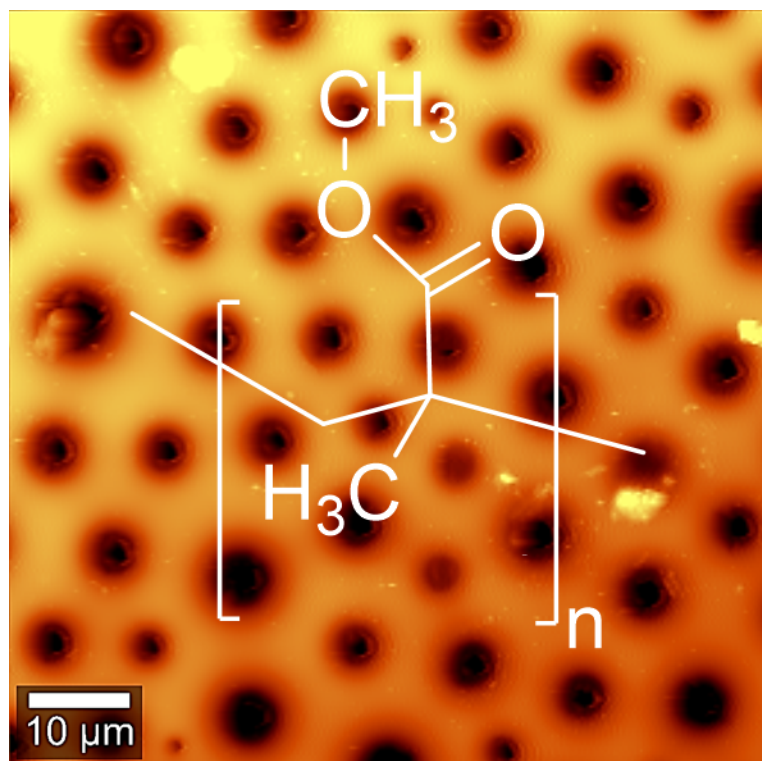
Fabrication of microporous PMMA using ionic liquids: an improved route to classical ScCO$_2$ foaming process

Miriam Trigo-López,[1] S. Vallejos,[1] José A. Reglero Ruiz,*[1] Cipriano Ramos,[2] Sagrario Beltrán,[2] Félix C. García,[1] and José M. García*[1]

[1] Departamento de Química, Facultad de Ciencias, Universidad de Burgos, Plaza de Misael Bañuelos s/n, 09001 Burgos, Spain. Tel: +34 947 258 085; Fax: +34 947 258 831.

[2] Departamento de Biotecnología y Ciencia de los Alimentos, Área de Ingeniería Química, Facultad de Ciencias, Universidad de Burgos, Plaza de Misael Bañuelos s/n, 09001 Burgos, Spain. Tel: +34 947 258 085; Fax: +34 947 258 831.

*Corresponding author E-mails: jareglero@ubu.es (José A. Reglero Ruiz) ; jmiguel@ubu.es (José M. García)

Abstract

The use of supercritical CO$_2$ (ScCO$_2$) has been established as a standard technique to produce micro- and nanocellular polymers with controlled morphologies and cell sizes between 500 nm and several microns. However, overcoming the gap between micro and nanocellular polymers implies the use of long saturation times (up to several days) and low temperatures (below 0 ºC) combined with high saturation pressures (above 30 MPa). This work presents a different approach to obtain microporous poly(methyl methacrylate) (PMMA) structures with controlled morphologies using a physical procedure employing ionic liquids that are mixed in solution with PMMA. The ionic liquid can produce interesting fine microporous materials simply by being removed with distilled water. The work compares the two fabrication methods previously mentioned to critically analyze the benefits and drawbacks of each preparation route. The ~~new~~ method in this paper opens the possibility to obtain microporous polymers by employing ionic liquids, thus reducing the time of processing, avoiding specific foaming equipment and broadening the applicability of crosslinked and semi crystalline polymers. Low velocity tensile test results are also presented to point out the improvement in the mechanical parameters of microporous films obtained from ionic liquids compared to those of films foamed using ScCO$_2$.

Keywords: ionic liquid; ScCO$_2$; microporous film; PMMA

1. Introduction

The production of micro- and nanocellular materials, specifically polymeric foams, has gained special interest in the last ten years due to their combination of low weight along with low thermal conductivity, acoustical isolation and high energy absorption [1,2]. Considering the polymeric materials, the classical production route to obtain micro and nanocellular morphologies uses the well-known supercritical CO_2 (ScCO_2) batch foaming process, which has been deeply described in the literature since the early 1990s [3,4]. In a single-step process, foaming occurs in a steel reactor in which the dense polymeric sample is placed. Then, after saturating the polymer with CO_2 above the critical point (31 ºC and 73 bar) for a variable period of time (from several hours up to one week), the reactor is quickly depressurized and produces a two-phase material (polymer foam). Following this route, different amorphous polymers and blends can be foamed, such as PMMA or polystyrene (PS), by taking advantage of the good solubility of CO_2 in most amorphous polymers [5]. Cell sizes in the range of 1 micron and densities of approximately 0.3 g/cm^3 can be obtained after the optimization of the foaming parameters (saturation pressure, temperature, time and depressurization rate) [6,7]. Although the use of ScCO_2 as a foaming agent presents great benefits compared to other chemical foaming methods (CO_2 is an inert gas, inexpensive and its critical conditions can be easily reached), it also has some limitations: it requires special equipment, the foamability of semicrystalline polymers is low and saturation times are usually long (from several hours up to days). Moreover, foaming parameters are directly related to the density reduction and the final morphology of the polymer foam; thus, a very accurate process control is needed to obtain specific microcellular polymers.

Among all the amorphous polymers, the foamability of PMMA under ScCO_2 has been widely analyzed due to it having several advantages; thus, PMMA is a commodity polymer with high CO_2 affinity and good mechanical and thermal properties. Recently, different works have reported the production of low-density materials with nanocellular morphologies, thus increasing their research interest [8,9]. On the other hand, there are some difficulties to note: first, reducing the cell size down to the nanometer scale usually implies the addition of a block copolymer, such as poly(methyl methacrylate)-poly(butyl acrylate)-poly(methyl methacrylate) (MAM), to a PMMA matrix [10] and second, due to the diffusion mechanism of CO_2 during the depressurization process, samples present a solid outer skin that must be mechanically removed to characterize

the intrinsic properties of the pore structure, for example, compression or tensile tests [11].

One of the most important difficulties to overcome is the low CO_2 affinity in engineering polymers, such as aromatic polyamides (aramids). In this sense, different approaches have been employed to improve both CO_2 absorption and foaming capability. One of these approaches is focused on the use of ionic liquids (ILs) due to their good compatibility combined with their enhancement of CO_2 absorption [12,13]. Our group recently developed a very promising technique in which commercial aramid films based on poly(*m*-phenylene isophthalamide) (MPIA) were effectively foamed through the ScCO$_2$ batch foaming process using ionic liquids (ILs) (1-allyl-3-methylimidazolium chloride) to nucleate and retain the CO_2 molecules [14]. We surprisingly observed that porous aramids could be fabricated by removing the IL in distilled water (avoiding the use of ScCO$_2$) [15], which simplified the mechanism to obtain porous structures and had not been previously reported in the literature [16]. This technique is similar to the salt leaching process, in which porous networks are created and optimized employing different salts (NaCl, NaHCO$_3$, etc.) and then eliminated after removal in distilled water. The salt leaching procedure has been successfully applied to produce polycaprolactone scaffolds composites [17,18] and porous biodegradable materials based on poly(*L*-lactic-co-glycolic acid) for biomedical applications [19]. In our case, the ionic liquid acts as a water-soluble phase, replacing the employed salt that is eliminated during the leaching process.

Following this idea, we extend our previous work to amorphous polymers, fabricating microporous PMMA films using ILs. Due to the good foamability of PMMA under ScCO$_2$, we compare the characteristics of porous films obtained from these two methods: the classical ScCO$_2$ foaming process and by fabricating polymer films with different proportions of IL using a simple cast process that is followed by the removal of the IL in distilled water. At the end, we will outline the main advantages of our process, such as simplicity, low processing times, the possibility of producing microporous structures in semicrystalline polymers and the avoidance of special equipment required for the ScCO$_2$ foaming process. Additionally, a full characterization of the materials obtained from both routes will be carried out, including cellular morphology, thermal properties, AFM-RAMAN tests and mechanical behavior.

Experimental part

1.1 Materials

The ionic liquid (IL) used was 1-allyl-3-methylimidazolium chloride (≥ 97 %) (Sigma-Aldrich, used as received), and *N,N*-dimethylacetamide (DMAc, Aldrich, > 99 %, used as received).

Two commercial PMMA powders (M_w ≈ 120,000 and 350,000 number average weight molar mass) were purchased from Sigma-Aldrich and used as received. PMMA with a lower molecular mass was designated PMMA-1, and PMMA with a higher molecular mass was named PMMA-2. The density values of the PMMA powders were 1.16 g/cm^3 for PMMA-1 and 1.17 g/cm^3 for PMMA-2.

2.2 Characterization methods

Cellular structural determination of the microporous polymeric films was carried out in with scanning electron microscopy (SEM) using a model FEI Quanta 600. Films were frozen in liquid nitrogen, fractured and gold coated in vacuum to assure the electrical conductivity of the films. Cellular structural characterization determining the average bubble radius $\bar{R}$ and average cell density from SEM images was measured using ImageJ® software and consisted of counting the number of bubbles in each image n_i and its radius R_i [20]. The average radius was calculated by means of Equation 1.

$$\bar{R} = \frac{\sum_{i=1}^{N} n_i R_i}{\sum_{i=1}^{N} n_i}$$

(1)

, where *N* represents the bubble count. Three different SEM images were analyzed from each material, and the data was averaged. The estimation of the cell density N_c was calculated using the Kumar's approximation, as shown in Equation 2.

$$N_c = \left(\frac{n}{A}\right)^{3/2}$$

(2)

, where *n* is the number of cells in the image and *A* is the area of the image. The description of the calculation method can be found in our previous work [21].

4

Density was determined from the dimensions and weight of the samples. In solid samples, thickness was determined directly using a digital micrometer, whereas in microporous films, thickness was measured from SEM images taken in the cross-section section to analyze the expansion rate.

Differential scanning calorimetry (DSC) was performed to evaluate the thermal transitions of the materials. Tests were carried out following a five-step cyclic procedure. First, after 5 min of stabilization at 30 ºC, films were cooled down to -80 ºC at 15 ºC/min. Then, the samples were stabilized for 5 min at -80 ºC and heated to 200 ºC to erase the thermal history. Then, a second cooling run down at -80 ºC was carried out at 5 ºC/min. Then, samples were again heated to 200 ºC at 15 ºC/min, and finally, samples were cooled down to RT at 5 ºC/min. All tests were performed under N_2 atmosphere (flow rate 50 ml/min), with a mass sample of approximately 15 mg.

The AFM-RAMAN images and spectra were taken using a confocal AFM-RAMAN model Alpha300R – Alpha300A AFM from WITec, using a laser wavelength of 532 nm with 2 mW at 100X with an AFM tip of 42 N/m. The area of the image was fixed at 75x75 μm^2. Images and spectra were taken at RT. Photographs of the surface of the samples were recorded with the same equipment, at 10X, 20X, 50X and 100X.

To determine the mechanical properties, 5 x 40 mm^2 strips were cut from the PMMA films, and tensile tests were performed on a SHIMADZU EZ Test Compact Table-Top Universal Tester. Mechanical clamps were used, and an extension rate of 5 mm/min was applied using a gauge length of 9.44 mm. At least 5 samples were tested for each film, and the data were then averaged. The Young's modulus and stress-strain values at break were obtained.

2.3 Fabrication of films

In the first step of the investigation, we prepared films by casting, using DMAc as the solvent. Two different groups of films were prepared. A first group of pure PMMA films was foamed using $ScCO_2$, and a second group of films, in which different proportions of IL were added to the PMMA to obtain a microporous structure by removing the IL from the films with distilled water, were obtained from casting.

a) Films prepared for $ScCO_2$ foaming

In the case of pure PMMA films for $ScCO_2$ experiments, 1 g of PMMA-1 was dissolved in 7 ml of DMAc and stirred until full dissolution. The mixture was then filtered off and cast in a glass placed inside an air-circulating oven at 60 ºC for 12 h. Four films were

fabricated following this route, one of which remained dense, and the other three films were foamed at three saturation temperatures (RT, 40 ºC and 60 ºC). Each film was then cut into two samples to obtain two foamed pieces from each test. The entire procedure was replicated using PMMA-2.

b) Films containing IL

Films with IL were fabricated as follows: three proportions of IL were selected (20, 30 and 40 wt.% with respect to PMMA). Then, quantities of IL and PMMA-1 powder were selected to obtain 1 g of total weight for each film. Each mixture of PMMA-1_IL was dissolved in 7 ml of DMAc and stirred until solution. As stated previously, the mixture was then filtered off and cast in a glass placed inside an air-circulating oven at 60 ºC for 12 h. Each film was then cut into two samples. The procedure was replicated for PMMA-2.

Table 1 presents the nomenclature and physical characteristics of the films. Additionally, two pure PMMA films (PMMA-1 and PMMA-2) were fabricated to compare their mechanical characteristics with the microporous samples obtained through IL removal and ScCO$_2$ foaming processes. Concerning the densities, they are approximately 1.15 g/cm^3 in samples without IL, whereas adding the IL reduces the density down to 0.99 g/cm^3 (in samples with 40 wt.% of IL). These experimental values reasonably agree with the density obtained from the rule of mixtures, considering the density of the IL as $\rho_{IL} \approx 0.92$ g/cm^3 (measured by us).

Table 1. Nomenclature and characteristics of the films fabricated.

Film	% PMMA	% IL	Thickness (µm)	Density (g/cm^3)	Route
PMMA-1 [1)]			111	1.13	Casting from DMAc
PMMA-2 [1)]			118	1.15	
PMMA-1_RT [2)]			93	1.17	Casting from DMAc followed by ScCO$_2$ foaming
PMMA-2_RT [2)]			97	1.13	
PMMA-1_40 [2)]	100	0	99	1.13	
PMMA-2_40 [2)]			102	1.14	
PMMA-1_60 [2)]			108	1.15	
PMMA-2_60 [2)]			99	1.14	
60PMMA-1_40IL [3)]	60	40	102	0.98	Casting from DMAc and IL and further
60PMMA-2_40IL [3)]			98	0.99	
70PMMA-1_30IL [3)]	70	30	103	1.02	

			91	1.03	removal of IL
70PMMA-2_30IL [3]			91	1.03	removal of IL with water
80PMMA-1_20IL [3]	80	20	97	1.07	with water
80PMMA-2_20IL [3]			96	1.09	

[1] Pure PMMA films (dense) ; [2] Pure PMMA films produced for $ScCO_2$ foaming at three saturation temperatures (RT, 40 ºC and 60 ºC) ; [3] PMMA_IL films containing 20 %, 30 % and 40 % wt. of IL.

Figure S1 of the Electronic Supporting Information (ESI) shows two photographs of the PMMA-1 and 60PMMA-1_40IL samples, evidencing that, although both samples show a good degree of transparency, sample with 40 % wt. of IL presents certain opacity, probably due to the presence of two different phases. Additionally, we observed a small increase of the opacity with respect to the proportion of IL. We believe that the opacity is uniquely related to the presence of a separated phase of IL, considering the transparency of pure PMMA films.

2.4 Production of the microporous films

Microporous films were obtained following the previously mentioned routes: $ScCO_2$ foaming and the removal of the IL. The experimental details of both routes are described below.

a) $ScCO_2$ foaming process

Foaming took place in a single-step batch process using $ScCO_2$ in a 2 L high-pressure steel reactor. Samples of 40 x 40 mm^2 were sandwiched between 2 square steel plates (50 x 50 mm^2 and 2 mm thickness) to confine the gas during depressurization, thus limiting the gas diffusion process outside the material [22]. Foaming tests were carried out at three different temperatures (RT, 40 ºC and 60 ºC). The saturation pressure was fixed at 35 MPa for 8 h in all cases. Depressurization was carried out using an on-off manual opening valve, with a depressurization time of approximately 10 s. Foamed films will be denoted with an *"f"* subscript using the same nomenclature presented in **Table 1**.

b) Removal of IL

Ionic liquid was eliminated by immersing the samples (40 x 40 mm^2) in distilled water for 24 h at 60 ºC in a three-step procedure, replacing the distilled water every 8 h. Then, the samples were dried at 60 ºC overnight to eliminate the remaining moisture.

Films after IL removal will be described with an *"r"* subscript, following the nomenclature presented in **Table 1**.

3. Results and discussion

For a better understanding of the scope of the work, the discussion of the results will be divided into two sections. In the first section, the information obtained by DSC and AFM-RAMAN is reported. In the second section, different properties of the microporous films obtained from both fabrication routes will be discussed from different points of view: morphology; in terms of structural parameters (pore size $\bar{R}$, pore density N_c and sample density ρ); distribution of the IL in the PMMA matrix and rugosity of the surface through AFM-RAMAN analysis; and finally mechanical properties from tensile tests.

3.1 Fabricated films

3.1.1 Thermal behavior

Before obtaining the microporous structures, thermal characterization of the films described in **Table 1** was carried out. DSC curves of pure PMMA films obtained in the second run are presented in **Figure S2** of the ESI. Pure PMMA-1 presents a T_g value of 120 ºC, and PMMA-2 shows a higher glass transition temperature (133 ºC) because of its higher M_w. In this sense, the dependence of T_g on molecular mass in PMMA has been studied by different authors. For example, Kabomo and Blum reported values of T_g between 116 and 133 ºC for PMMAs with molecular masses between 10^4 and 10^5 [23]. Roth *et al.* described the dependence of the glass transition temperature on molecular mass in PMMA thin films, with values between 110 ºC and 120 ºC for molecular masses of approximately 10^3 and 10^4 [24]. More recently, Geng and Tsui described a similar glass transition behavior in PMMA thin films when the molecular mass was increased [25].

The thermal behavior of IL is presented in **Figure S3** of the ESI. In the first run, an endothermic peak at 55 ºC corresponded to the melting point of the crystalline phase of the IL. In the second run, only a glass transition region is detected at -55 ºC. It is important to say that several runs were performed at low cooling rates, and no crystallization was observed.

Finally, **Figures S4** and **S5** of the ESI show the thermograms of PMMA_IL films obtained during the second heating run. Three different transitions are detected, with a similar behavior in PMMA-1- and PMMA-2-based films. Transition 1 corresponds to the

glass transition of the IL. The second transition corresponds to the melting point of the IL, and finally, transition 3 is the glass transition of the PMMA. Thus, it is clear that the thermal behavior of the IL and PMMA can be analyzed separately in the PMMA_IL films, which indicates that no mixing has occurred and phases are separated in the entire range of temperatures analyzed (from -50 ºC to 150 ºC). **Table S1** in the ESI presents the thermal parameters extracted from the PMMA_IL DSC curves, including the glass transition and melting point of the IL, together with the glass transition of the particular PMMA. The values do not differ from the parameters detected in pure materials, thus reinforcing the idea of the IL and PMMA phase separation in the films.

3.1.2 IL distribution in the PMMA matrix

AFM-Raman tests were carried out in fabricated films with IL to analyze the PMMA_IL phase distribution and study the correlation between the removal of the IL with the porous morphology. **Figure 1** presents different optical photographs of the surface of PMMA_IL in all the fabricated films.
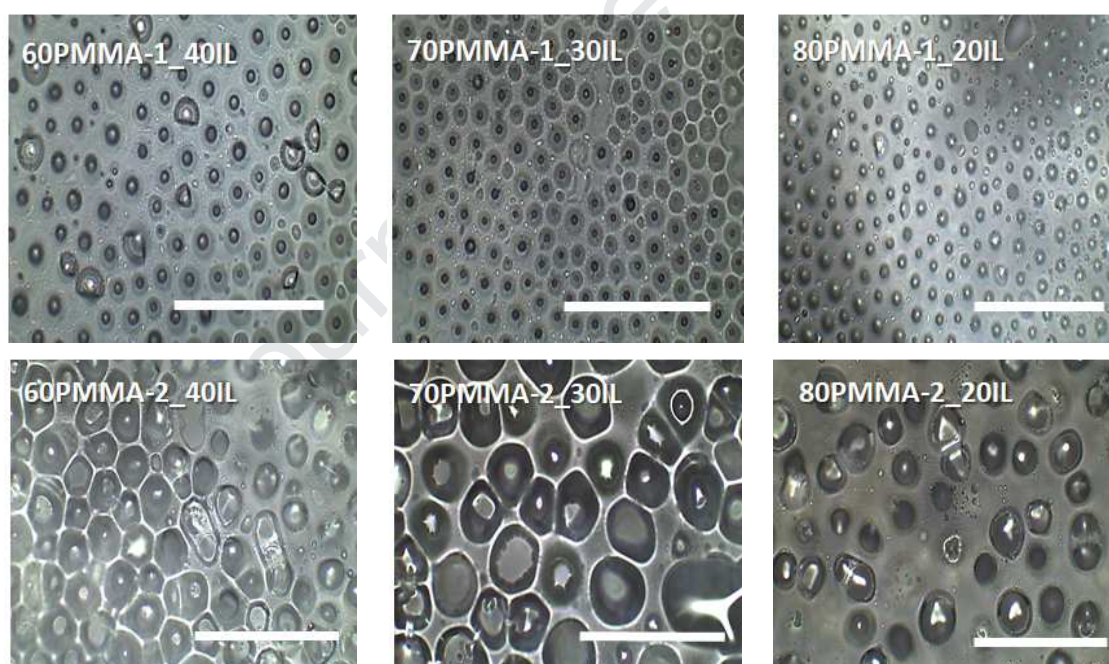
Figure 1. Optical micrographs of the surface of the fabricated films with ionic liquids. Bar scale 200 µm.

Having a look at the optical photographs, a very different IL distribution can be detected in the PMMA matrix, thus indicating a strong influence of the PMMA molecular mass employed in the formation of PMMA_IL phases. First, complete segregation of the PMMA and the IL, which are distributed in separated phases, is evidenced. This observation agrees with the DSC results presented in **Figures S4 and S5** of the ESI.

Concerning low molecular mass PMMA-1 ($\approx$ 120,000 number average weight molar mass), the IL is distributed in isolated droplets of circular shape, with sizes of approximately 15-20 μm. In the case of higher molecular mass PMMA-2 ($\approx$ 350,000 number average weight molar mass), adding 20 wt.% of IL produces isolated droplets of a large size ($\approx$ 40 μm). Increasing the IL content also increases the number of droplets, with sizes above 50 μm.

The segregation of the IL in the PMMA matrix can also be analyzed by collecting localized RAMAN spectra in different regions of the two-phase system. For this purpose, RAMAN spectra of an IL droplet and of the PMMA matrix were obtained from a 60PMMA-1_40IL film and compared with the RAMAN spectra data obtained from the pure PMMA-1 and IL. Figures S6 and S7 of the ESI confirm that both the RAMAN spectra of the film and the IL are similar, confirming the phase separation also observed in the optical micrographs and in the DSC results. In addition, this phase separation could be the reason for the opacity observed in PMMA films containing IL, as indicated in section 2.4 b).

The phase separation of PMMA and IL during the film formation is due to the non-compatibility of the two materials. In our procedure, the DMAc (solvent) acts as a compatibilizer during the solution process, but when the solvent is evaporated, PMMA and IL segregates in two separated phases, as shown in the optical micrographs presented in **Figure 1**. We believe that PMMA and IL segregate in different phases because they are not compatible after solvent evaporation, as can be deduced from their solubility parameters. The Hildebrand solubility parameter of DMAc was taken as δ_H = 22.7 (MPa)$^{1/2}$ [26]. In the case of PMMA, the value of δ_H was approximately 18 (MPa)$^{1/2}$. It is reported that PMMA presents good solubility in solvents with δ_H between 16 and 28 (MPa)$^{1/2}$, thus explaining the miscibility of PMMA and DMAc [27].

Although the solubility of different ILs has been analyzed in the last years [28], in the case of our specific IL, we only found a reference in which the Hildebrand solubility parameter was measured at different temperatures from 343 to 373 K [29], extrapolating the value of δ_H at RT to 26.5 (MPa)$^{1/2}$. This value is slightly higher than the solubility parameter DMAc but much higher than the solubility parameter of PMMA. Taking into account these values, it could be justified that PMMA, IL and DMAc are soluble due to the proximity of the solubility parameters of PMMA and IL to the solubility value of DMAc. However, when DMAc is evaporated, the difference between the solubility parameters of PMMA and IL is high enough to reduce their miscibility and to promote the phase separation.

Moreover, the surface porosity depends not also on the IL quantity, but on the molecular weight of the PMMA employed. As shown in **Figure 1**, the size of the IL droplets in films with PMMA 2 ($\approx$ 350,000 number average weight molar mass) is higher than the observed in PMMA 1 films ($\approx$ 120,000 number average weight molar mass). It is clear that increasing the molecular mass of the PMMA requires a lower difference between the solubility parameter of PMMA and that of the solvent to assure miscibility, as we also detected experimentally. This is due to several reasons. First, the structural units which need to be solvated by the solvent cannot have an unlimited number of configurations in space as a low molecular mass solute can attain. Also, the increase in molecular mass increases the cohesive energy density (CED), and the solubility parameter depends on the square root of the CED. Finally, the rise of entanglements with increasing molecular mass lowers the solubility due to the reduction of the mobility of the molecular chains [30].
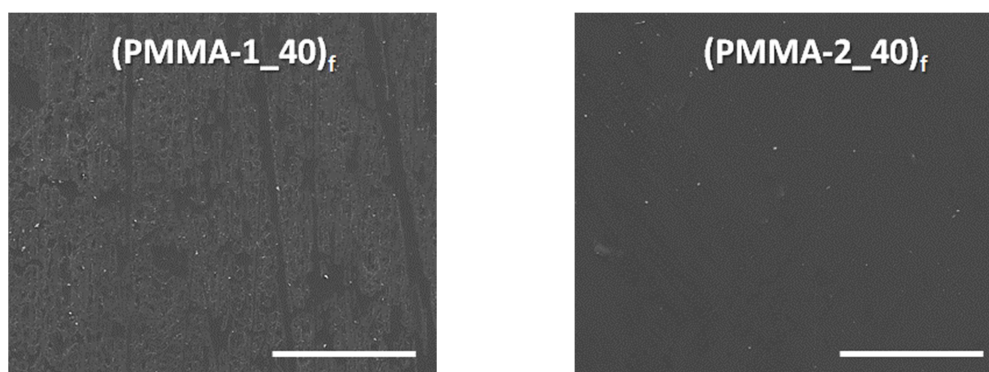
3.2 Microporous films

3.2.1 Morphology

a)   Foamed films using ScCO$_2$

SEM micrographs of the microporous films obtained from the ScCO$_2$ foaming process are presented in **Figure 2** (cross-section) and **Figure 3** (surface).
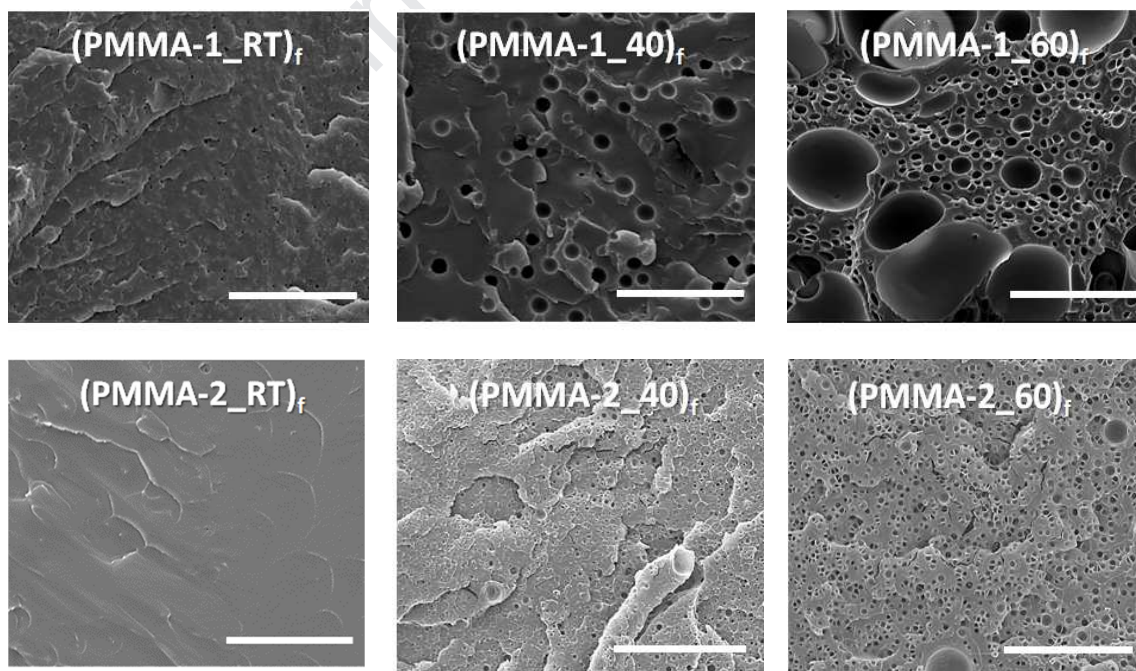
Figure 2. SEM micrographs of the cross-section of the porous films curves of PMMA-1 and PMMA-2 films produced by ScCO$_2$ foaming process. Bar scale 20 μm.

11

Figure 3. SEM micrographs of the surface of porous PMMA films fabricated through the ScCO$_2$ foaming process (saturation temperature 40 ºC). Bar scale 50 μm.

From the analysis of the SEM micrographs of the cross-section (**Figure 2**), different conclusions can be obtained. When films are saturated at RT, no foaming occurs. On the other hand, increasing saturation temperatures at 40 ºC enhances foamability, and some isolated pores appear in PMMA-1 film, whereas PMMA-2 film shows a much more homogeneous pore structure. At 60 ºC, both PMMA films present the typical closed-cell morphology, with a bimodal size distribution that usually appears in PMMA and polycarbonate (PC) foams [31]. It is important to note that in all the cases PMMA-1 presents an average pore radii higher than PMMA-2 films. Concerning the surface porosity, **Figure 3** shows two micrographs of the surface of PMMA-based foamed films fabricated at 40 ºC of saturation temperature. As it can be seen, films present an outer solid skin, a classical structure derived from the rapid diffusion of the CO$_2$ from the external part of the films [11]. Films saturated at RT and 60 ºC show a similar behavior.

~~Foaming behavior of amorphous polymers can be explained through the plasticization effect, in which the determination of the glass transition temperature under ScCO$_2$ plays a key role. It is well known that the glass transition of amorphous polymers decreases with saturation pressure, thus allowing their CO$_2$ sorption and subsequently their foamability. Different authors have described experimentally the plasticization of several polymers in presence of compressed fluid diluents, such as Condo *et al.* [32] or Zhang *et al.* [33] For example, focusing on polystyrene, Alessi *et al.* [34] presented a study of the plasticization effect in polystyrene by high pressure partition chromatography, comparing the experimental results with data available in the literature. Results showed how T_g is reduced 40 ºC at saturation pressures of only 8 MPa.~~

A more accurate expression was developed by Hwang *et al.* [35], analyzing the relationship between gas absorption and the glass transition temperature in a batch microcellular process through the measurement of the elasticity modulus induced near the glass transition temperature. Hwang compared experimental data with Chow's model, proposing a new expression as a function of weight gain ratio during the saturation process (equation 3).

$$T_g = T_{g,0} exp\left[-\left(M_p\right)^{-1/3}(\rho)^{-1/4} \cdot \alpha \cdot w\right] \tag{3}$$

, where M_p is the molecular mass of each PMMA, $T_{g,0}$ are the glass transition temperatures of each PMMA determined at ambient pressure through the DSC curves, α is a material constant determined by both polymer and gas and ρ is the specific density of the polymer.

M_p and $T_{g,o}$ are known parameters, but α and w must be determined independently. In the case of α constant, typical values for amorphous polymers and CO_2 vary between 0.7 and 0.8. In our case, we perform the calculations using both values, and we did not observe any difference, then choosing a final value of α = 0.75. In the case of w (weight ratio of CO_2 absorbed), the precise determination must be carried out in the reactor, using a magnetic balance, before the depressurization process. [36] In our case, we simply measured the weight of each film just after extracting the samples from the reactor. Thus, this value must be considered an approximation, assuming that the exact percentage of CO_2 absorbed must be higher. **Figure 3** shows the predicted plasticized glass transition temperatures of each PMMA in the three foaming tests (each PMMA shows six points because two samples were foamed at each temperature), together with the saturation temperature of each experiment.
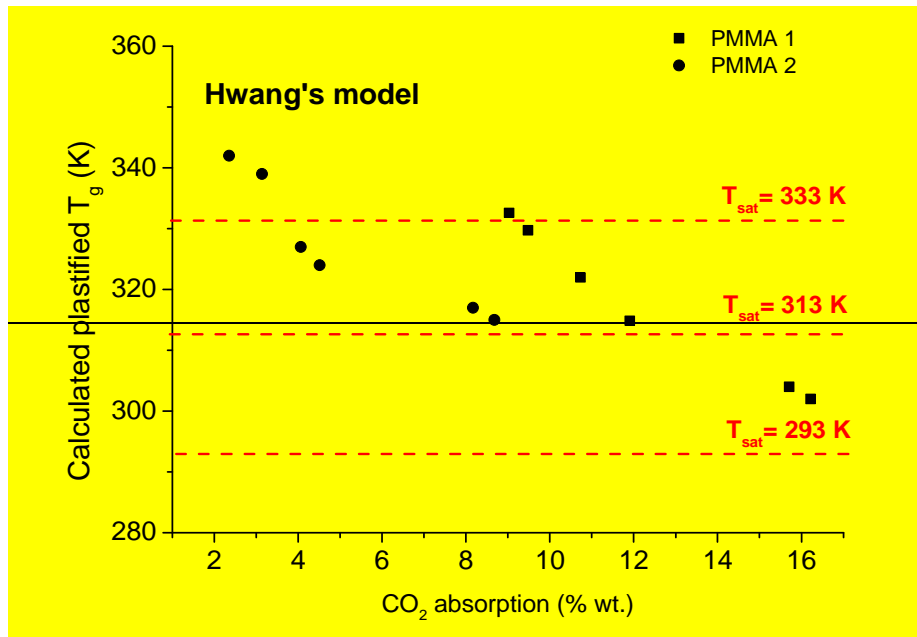
Figure 3. Calculated plasticized glass transition temperatures for PMMA-1 and PMMA-2 films according to Hwang's model.

As it can be seen in **Figure 3**, in foaming tests at RT (293 K), PMMA-1 is plasticized down to 305 K, whereas PMMA-2 shows a T_g of 320 K. In the second foaming test, at 313 K, PMMA-1 shows a T_g around 315 K, and PMMA-2 is plasticized down to 325 K. Finally, in the last foaming test at 333 K, PMMA-1 is plasticized down to 330 K and PMMA-2 presents a T_g around 340 K. Having a look at the results, we can define for each PMMA a "gap temperature", T_{gap}, as the difference between the plasticized glass transition T_g and the saturation temperature T_{sat}, as described in **Table 2**.

Table 2. Values of gap temperatures for PMMA-1 and PMMA-2 films.

Sample	T_{sat} (K)	T_g (K)	T_{gap} (K)
PMMA-1	293	305	12
PMMA-2		320	27
PMMA-1	313	315	2
PMMA-2		325	12
PMMA-1	333	330	-3
PMMA-2		340	7

Values in **Table 2** explain numerically the foaming behavior of PMMA films. When films are saturated at RT, foaming temperature is below plasticized T_g for both PMMA-1 and

~~PMMA-2, and no foaming occurs. Increasing saturation temperature decreases the gap, then enhancing the foamability of PMMA films. When films are saturated at 333 K, gap is practically negligible, then obtaining the closed-cell morphologies observed in the SEM micrographs in **Figure 1**.~~

b) Microporous films obtained after IL removal from films containing IL

Microporous films produced using ILs show a very different morphology. **Figure 4** presents the SEM micrographs of the cut section of microporous PMMA films after the removal of the IL in distilled water. In all cases, films present a well-defined closed-cell morphology with homogeneous pores. Compared to $ScCO_2$ films, the IL easily promotes the formation of the porous structure. ~~avoiding the plasticization problems exposed previously~~. On the other hand, it can be seen that pore size does not vary greatly with the quantity of the IL, although PMMA-2-based films show large pores with an elongated shape, whereas in films produced from PMMA-1 pores present a circular shape.

It is important to say that the literature concerning the fabrication of porous materials using ionic liquids presents interconnected porous structures (scaffolds) with channels through with liquid is dissolved in the distilled water [17,18,19]. In our case, we believe that the temperature of the distilled water during the removal process (80 °C, 24h) melts the ionic liquid, and it can slowly diffuse through the solid PMMA matrix. The melting temperature of the ionic liquid was determined by DSC ($T_m \approx 55$ °C, see **Figure S3 of the ESI**). On the other hand, the diffusion time of the melted IL through the PMMA matrix could be a longer process in bulk samples. To verify that all the IL was effectively removed from the films, **Figures S8** and **S9** of the ESI present the TGA curves of 60PMMA_40IL films before and after IL removal, showing the disappearance of the weight loss associated with the IL.

A narrow pore distribution was also observed with regular cells of similar diameter. In our case, the pore size is directly defined by the IL droplet, in which pore structure is originated during the removal of IL in distilled water. Concerning the formation of the IL droplets, we believe that our method allows the formation of a regular IL distribution due to the slow solvent evaporation process (60 °C during 12 h), in contrast to that of similar procedures of pore formation in polymers. For example, in thermally induced phase separation processes, the cooling rate has a predominant effect in the pore structure [37,38]. Also, in $ScCO_2$ foaming processes, the depressurization rate greatly affects to the pore morphology [39]. In this work, the slow solvent evaporation originates IL droplets of similar size, and subsequently, a regular pore morphology.

15
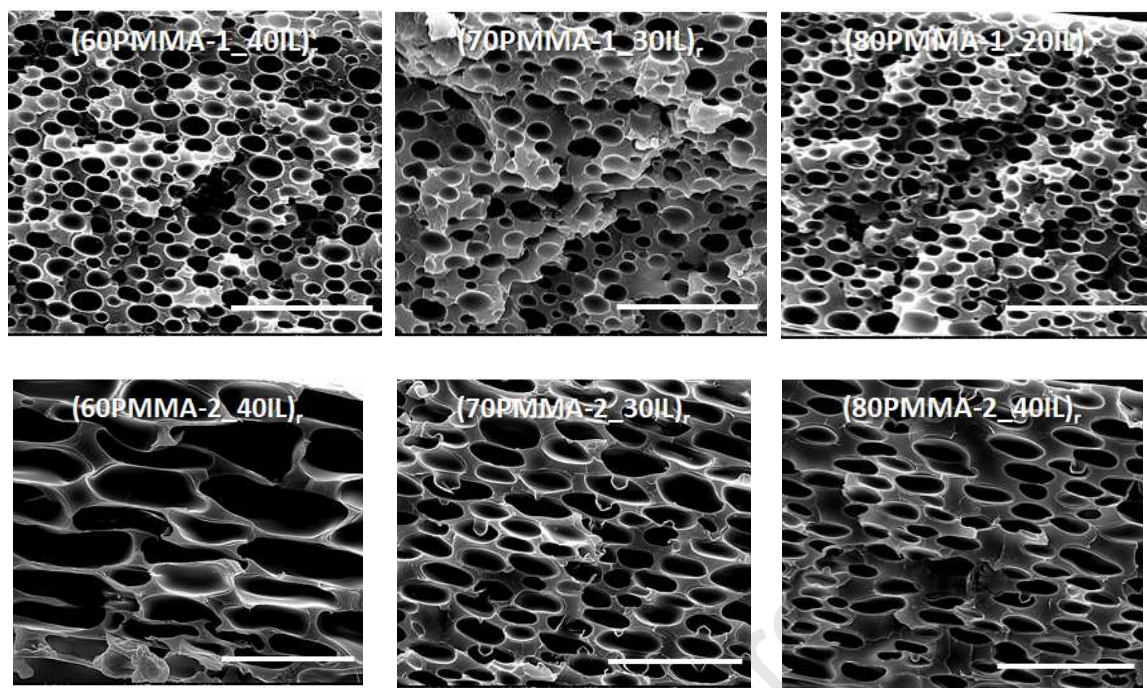
Figure 4. SEM micrographs of the cut section of the porous films curves of PMMA-1 and PMMA-2 films after the removal of the IL. Bar scale 20 μm.

Additionally, **Figure 5** collects the SEM micrographs of the surface of microporous films, in which a regular pore distribution is evidenced. It is important to note that in samples foamed using $ScCO_2$, a solid outer skin was observed in all the samples. It is clear that the use of ILs also promotes the formation of surface porosity, thus opening the possibility of using these films in different applications in which a high specific surface area is required. Surface porosity is dependent on the PMMA employed and on the quantity of IL. Micrographs show that PMMA-1-based films present lower pore sizes than PMMA-2 films. Moreover, increasing the quantity of IL up to 40 wt.% reduces the number of pores (pore density) and slightly increases the pore size compared to films with 20 wt.% of IL.
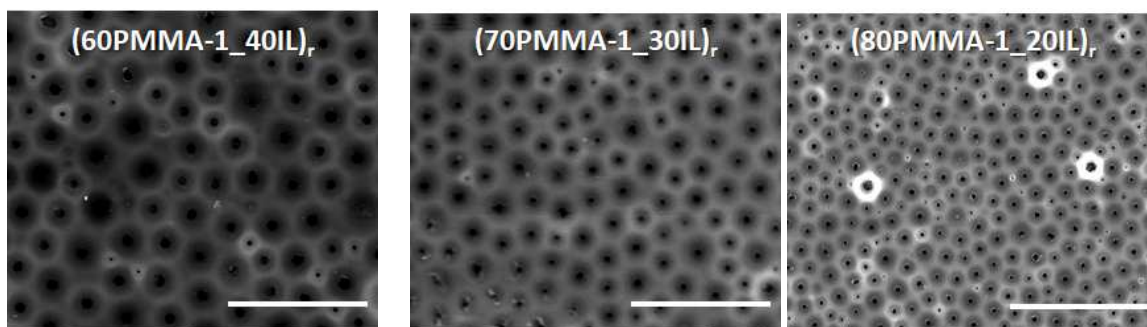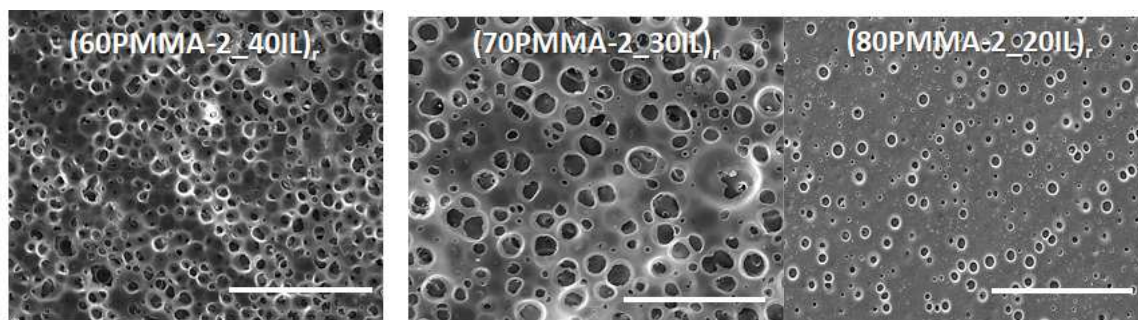
Figure 5. SEM micrographs of the surface of the porous films curves of PMMA-1 and PMMA-2 films after the removal of the IL. Bar scale 50 μm.

Comparing the PMMA_IL phase distribution in fabricated films to the surface morphology of microporous films after IL removal, it is possible to correlate the IL size and distribution with the pore density and size in the surface of the films. Data are listed in **Table S2** of the ESI, comparing the PMMA_IL phase morphology in terms of droplet size and droplet density using ImageJ® software, with the microporous parameters calculated using the same software. The linear correlation is represented in **Figure S10** of the ESI for both parameters with good fitting parameters in both cases ($r^2 \approx 0.96$).

c) Comparison of microporous morphologies

The morphological analysis of microporous films produced by both routes is presented in **Table 2,** which presents the structural parameters obtained from the SEM micrographs **(Figures 2, 3, 4** and **5)**. It is observed that films produced using ScCO$_2$ are only foamed at saturation temperatures of 40 ºC and 60 ºC due to the plasticization phenomenon. The pore sizes are between 1 and 5 μm, but a strong bimodal distribution is observed at 60 ºC of saturation temperature, as reflected in the high value of the standard deviation associated with pore size measurement. Concerning the surface porosity, a solid outer skin is detected in all cases. The density of films varies between 0.74 and 0.98 g/cm^3, with a maximum reduction ratio of 35 %.

Microporous films obtained after the removal of IL present pore sizes slightly higher (between 4 and 15 μm) but with great homogeneity in all cases (standard deviation values are lower when compared to those of ScCO$_2$ films). Moreover, a defined porous morphology is obtained in all cases. The greatest difference arises in the surface aspect, presenting a close-cell porous morphology with sizes between 2 and 21 μm. The density is also lower in these films, with values between 0.42 and 0.71 g/cm^3, then reaching reduction ratios of 60 %.

Table 2. Morphological parameters of the microporous films.

Sample	Cut Section		Surface		Density (g/cm^3)
	$\bar{R}$ (µm)	N_C (cm^{-3})	$\bar{R}$ (µm)	N_C (cm^{-3})	
(PMMA-1_RT)$_f$	Not foamed	Not foamed			1.13
(PMMA-2_RT)$_f$	Not foamed	Not foamed			1.15
(PMMA-1_40)$_f$	2 ± 0.21	1.17·10^9			0.98
(PMMA-2_40)$_f$	1 ± 0.06	5.18·10^{10}	Outer solid skin		0.86
(PMMA-1_60)$_f$	5 ± 3.11	1.31·10^{10}			0.74
(PMMA-2_60)$_f$	1 ± 0.44	4.14·10^{11}			0.81
(60PMMA-1_40IL)$_r$	4 ± 0.03	1.05·10^{10}	5 ± 0.02	4.14·10^8	0.42
(60PMMA-2_40IL)$_r$	15 ± 1.81	1.31·10^9	12 ± 1.27	1.73·10^8	0.44
(70PMMA-1_30IL)$_r$	5 ± 0.08	8.03·10^9	7 ± 0.09	5.19·10^8	0.51
(70PMMA-2_30IL)$_r$	9 ± 2.12	5.72·10^9	21 ± 3.14	1.23·10^8	0.53
(80PMMA-1_20IL)$_r$	4 ± 0.11	1.47·10^{10}	2 ± 0.03	8.68·10^8	0.68
(80PMMA-2_20IL)$_r$	8 ± 1.35	4.69·10^9	8 ± 1.16	6.85·10^7	0.71

3.2.2 Surface aspect and rugosity

The surface aspect of microporous films is first evidenced in two photographs, which compare the aspect of the films after ScCO$_2$ foaming and removal of IL (**Figure S11** of the ESI). **Figure S11a** shows the PMMA-1_60 film, in which the surface has a strong rugosity compared to the smooth surface of the fabricated film (see **Figure S1a**). On the other hand, this could be related to the microporous formation process. When using ScCO$_2$, porosity is generated during the depressurization process, in which the film is brought under great thermal and mechanical stress (from 35 MPa to ambient pressure in 10 s, reaching temperatures of -30 ºC at the end of the process). When using IL, both the film fabrication and porous formation processes are much less harmful for the integrity of the film (see **Figure S11b**), involving low temperatures (60 ºC) at ambient pressure.

AFM images and rugosity profiles were also analyzed to study the surface of microporous films. Figures **S12** and **S13** of the ESI show AFM images taken from the (70PMMA-1_30IL)$_r$ and (PMMA-1_40)$_f$ films. Considering the surface of the microporous film obtained after IL removal (**Figure S12**), a regular pore distribution is observed, as detected from the SEM micrographs presented in **Figure 5**. Two different

rugosity profiles are traced (blue and green lines), in which the depth of the pores is estimated (approximately 2-3 μm). The colorimetric scale of the AFM image shows a smooth surface in the solid region of the film.

A very different behavior is observed on the surface of the foamed film under ScCO$_2$ (**Figure S13**). First, no porosity is observed, confirming the SEM observations presented in **Figure 2**. However, the colorimetric scale and rugosity profiles that are traced (blue and green lines) present a much rougher surface, with continuous height variations in the range of 2-3 μm. This analysis confirms that our procedure (involving the removal of IL) not only produces a regular surface porosity but also a much smoother surface compared to classical ScCO$_2$ foaming processes.

3.2.3 Tensile tests

The mechanical properties of the PMMA films were tested by analyzing the relative Young's moduli (E_r) and relative stress at break point (σ^{bp}_r), (ratio between measured values and film density, extracted from the data in **Table 1**). Relative values were employed to effectively compare the mechanical behavior of the microporous films and dense films obtained from the two commercial PMMAs. All the stress-strain curves obtained in the tensile tests can be found in **Figures S14** and **S15**, whereas the mechanical data are presented in **Table 3**.

Table 3. Mechanical properties of PMMA films obtained from the tensile tests. (E_r is the relative Young's modulus and σ^{bp}_r is the relative stress at break point).

Sample	E_r (MPa/(g/cm^3))	σ^{bp}_r (MPa/(g/cm^3))
PMMA-1	1803 $\pm$ 114	30 $\pm$ 2
PMMA-2	1916 $\pm$ 178	50 $\pm$ 6
(PMMA-1_RT)$_f$	984 $\pm$ 76	21 $\pm$ 1
(PMMA-2_RT)$_f$	1250 $\pm$ 134	27 $\pm$ 2
(PMMA-1_40)$_f$	1122 $\pm$ 118	18 $\pm$ 1
(PMMA-2_40)$_f$	1216 $\pm$ 127	31 $\pm$ 3
(PMMA-1_60)$_f$	902 $\pm$ 87	21 $\pm$ 3
(PMMA-2_60)$_f$	948 $\pm$ 99	15 $\pm$ 1
(60PMMA-1_40IL)$_r$	2004 $\pm$ 196	61 $\pm$ 4
(60PMMA-2_40IL)$_r$	2695 $\pm$ 256	82 $\pm$ 3

19

(70PMMA-1_30IL)$_r$	2309 ± 203	62 ± 5
(70PMMA-2_30IL)$_r$	2426 ± 211	66 ± 4
(80PMMA-1_20IL)$_r$	2658 ± 301	47 ± 4
(80PMMA-2_20IL)$_r$	2233 ± 276	48 ± 4

From the data presented in **Table 3**, different conclusions can be drawn. First, dense PMMA films present similar values of E_r (1803 and 1916 MPa/(g/cm^3)), although the stress at break point $\sigma^{bp}{}_r$ is significantly higher for dense PMMA-2 film (29.9 and 50 MPa/(g/cm^3)). This tendency can also be observed in all the microporous films (except in PMMA_60 films, but this could also be due to a density effect). Thus, it seems that increasing the molecular mass of PMMA generally enhances the stress at the break point.

Mechanical data of microporous foamed films using ScCO$_2$ reflect poor behavior compared to dense films. In terms of the relative Young's modulus E_r, the values vary between 902 and 1250 MPa/(g/cm^3), which are 1.5 and 2 times lower than that of the values measured in dense films. Specifically, films obtained at 60 ºC of saturation temperature present lower E_r values, probably due to the negative influence of the bimodal porosity observed in the SEM micrographs (**Figure 2**). Considering the stress at break point, all foamed samples show lower values than in dense films, except for film PMMA-2_40, which presents the finest pore structure (pore size below 1 μm and $\sigma^{bp}{}_r$ = 31.4 MPa/(g/cm^3)). Thus, it can be drawn that foamed films using ScCO$_2$ present lower mechanical properties than those of dense films.

The most interesting results emerge from the mechanical data of microporous films obtained by removing the IL. The relative Young's modulus values E_r are in the same range as that of the dense films, and in some cases, they are considerably higher (E_r values are higher than 2000 MPa/(g/cm^3) in the six films, reaching 2659 MPa/(g/cm^3) in the 60PMMA-2_40IL film. The relative strength of the dense film is increased when the microporous structure originates from using an IL. Compared to those of foamed films, films derived from an IL removal show the relative Young's modulus values as being twice as high. Additionally, the stress at break point is remarkably increased in microporous films derived from an IL, with values between 47.6 and 82.1 MPa/(g/cm^3), much higher than those values obtained in dense and foamed films.

20

There could be different reasons to explain these differences. First, it seems that the surface porosity has a positive effect on the mechanical data. Second, microporous samples obtained from an IL present lower density values, which then increase the relative magnitudes. Third, the microporous formation process using an IL can be described as a slow and gentle route, avoiding the thermal and mechanical stress associated with the use of $ScCO_2$, which could affect the mechanical performance of the film. Additionally, the presence of bimodal morphologies in films obtained from $ScCO_2$ has a negative influence on the mechanical behavior, and the use of an IL leads to homogeneous microporous distribution, enhancing the stress-strain curves.

The enhancement of the mechanical behavior due to the presence of the porosity has already been observed in the previous works of our group, in which microporous aramids were produced using ionic liquids presented relative Young's moduli and stress at break point values higher than those expected considering only the density reduction [14,15]. In this sense, the isolated effect of the cell-size reduction down to micro- and nano scale on the mechanical behavior has already been measured but has not been accurately modeled. The positive effect of micro- and nanoporosity is analyzed in some recent references concerning the mechanical properties of micro and nano-cellular polymers, in which the cell-size reduction to micro- and nanocellular scales enhances the values of different mechanical properties [40, 41, 42]. However, as has been said, this is still an open question because the classical modelling of mechanical properties of cellular materials (applied to cell sizes above 10-20 μm) are not 100 % valid at the micro- and nano scale.

3.2.4 Comparison keynotes of both routes

Bearing all these ideas in mind, we list in **Table 4** the main benefits and drawbacks of both production routes to briefly resume the key points analyzed in this research work.

Table 4. Comparative aspects (benefits and drawbacks) of $ScCO_2$ foaming and IL removal routes.

Process	Benefits	Drawbacks
ScCO₂	Use of inert gas, is a green process involving no solvents. Literature since early 90's. Great variety of amorphous polymers and	A special equipment is needed to produce $ScCO_2$ foamed films. Exigent processing conditions in terms of pressure and/or temperature.

	blends can be processed.	Saturation times can take several days. Higher density than microporous films obtained from IL removal (presence of an outer solid skin) Lower mechanical properties than microporous films produced from IL removal.
ILs	Simple and easy process, which could be applied also to semi crystalline polymers using appropriate solvents. Obtention of controlled surface porosity in terms of the IL distribution. Smoothness of the surface of the films. Lower density than ScCO$_2$ foamed samples. Improved mechanical properties.	The process must be tested in thick samples. It is necessary to use solvents. Polymer and IL must be solubilized in the organic solvent to obtain handleable films.

4. Conclusions

Here, we describe the production of microporous PMMA films ~~from a novel route,~~ employing IL as porosity promoters. The work is also intended to critically compare this route to the classical foaming process using ScCO$_2$. For this purpose, two commercial PMMAs of different molecular masses were employed, using 1-allyl-3-methylimidazolium chloride as an IL.

It was found that using this specific IL allows the production of regular morphologies in all the cases analyzed, with cell sizes in the range of several microns. However, foaming PMMA with ScCO$_2$ is only possible at high saturation temperatures (> 40 ºC) due to the plasticization effect. Moreover, bimodal morphologies were found in foamed PMMA samples, which negatively affected mechanical properties.

It was also observed that the PMMA_IL system formed a segregated two-phase structure. Removing the IL also provided a porous surface with a homogeneous morphology that was directly derived from the IL droplets removed by distilled water; thus, this process opens the possibility of estimating the characteristics of the surface porosity in terms of a two-phase distribution. Finally, tensile tests revealed a remarkable mechanical behavior of microporous films derived from an IL in terms of the relative Young's modulus and stress at break point, with values comparable or even higher than those of the parameters measured in dense films. It is clear that using an IL

22

can be a very promising route to obtain microporous polymers with controlled morphologies and improved mechanical properties.

References

[1] B. Notario, J. Pinto, M.A. Rodríguez-Pérez, Towards a new generation of polymeric foams: PMMA nanocellular foams with enhanced physical properties, Polymer 63 (2015) 116-126. https://doi.org/10.1016/j.polymer.2015.03.003.

[2] V. Bernardo, J. Martín de León, M.A. Rodríguez-Pérez, Production and characterization of nanocellular polyphenylsulfone, Mater. Lett. 178 (2016) 155-158. http://dx.doi.org/10.1016/j.matlet.2016.05.002.

[3] V. Kumar, Microcellular polymers: Novel materials for the 21st century, Progress in Rubber & Plastic Technology 9 (1993) 54-70.

[4] A.I. Cooper, Porous materials and supercritical fluids, Adv. Mater 16 (2003) 1049-1059. https://doi.org/10.1002/adma.200300380.

[5] K.F. Webb, A.S. Teja, Solubility and diffusion of carbon dioxide in polymers, Fluid Ph. Equilibria 158 (1999) 1029-1034. https://doi.org/10.1016/S0378-3812(99)00153-3.

[6] J.A. Reglero Ruiz, M. Pedros, J-M. Tallon, M. Dumon, Micro and nano cellular amorphous polymers (PMMA, PS) in supercritical CO_2 assisted by nanostructured CO_2-philic block copolymers – One step foaming process, J. Supercrit. Fluid. 58 (2011) 168-176. https://doi.org/10.1016/j.supflu.2011.04.022.

[7] J.A. Reglero Ruiz, J-M. Tallon, M. Pedros, Two-step micro cellular foaming of amorphous polymers in supercritical CO_2, J. Supercrit. Fluid. 57 (2011) 87-94. https://doi.org/10.1016/j.supflu.2011.01.011.

[8] J. Martín de León, J.L. Pura, V. Bernardo, M.A. Rodríguez-Pérez, Transparent nanocellular PMMA: Characterization and modelling of the optical properties, Polymer 170 (2019) 16-23. https://doi.org/10.1016/j.polymer.2019.03.010.

[9] V. Bernardo, J. Martín de León, J. Pinto, T. Catelani, A. Athanassiou, M.A. Rodríguez-Pérez, Low-density PMMA/MAM nanocellular polymers using low MAM contents: Production and characterization, Polymer 163 (2019) 115-124. https://doi.org/10.1016/j.polymer.2018.12.057

[10] V. Bernardo, J. Martín de León, E. Laguna-Gutiérrez, T. Catelani, J. Pinto, A. Athanassiou, M.A. Rodríguez-Pérez, Polymer 153 (2018) 262-270. https://doi.org/10.1016/j.polymer.2018.08.022.

[11] J. Martín de León, V. Bernardo, M.A. Rodríguez-Pérez. Low density nanocellular polymers based on PMMA produced by gas dissolution foaming: Fabrication and cellular structure characterization, Polymers 8 (2016) 265. https://doi.org/10.3390/polym8070265.

[12] A. Wilke, J. Yuan, M. Antonietti, J. Weber, Enhanced carbon dioxide adsorption by a mesoporous poly(ionic liquid), ACS Macro Lett. 1 (2012) 1028-1031. https://doi.org/10.1021/mz3003352.

[13] J. Cota, F. Fernández Martínez, Recent advances in the synthesis and applications of metal organic frameworks doped with ionic liquids for CO_2 adsorption, Coord. Chem. Rev. 351 (2017) 189-204. https://doi.org/10.1016/j.ccr.2017.04.008.

[14] B.S. Pascual, M. Trigo-López, C. Ramos, M.T. Sanz, J.L. Pablos, F.C. García, J.A. Reglero Ruiz, J.M. García, Microcellular foamed aromatic polyamides (aramids). Structure, thermal and mechanical properties, Eur. Polym. J. 110 (2019) 9-13. https://doi.org/10.1016/j.eurpolymj.2018.11.007.

[15] B.S. Pascual, M. Trigo-López, J.A. Reglero Ruiz, J.L. Pablos, J.C. Bertolín, C. Represa, J.V. Cuevas, F.C. García, J.M. García, Porous aromatic polyamides the easy and green way, Eur. Polym. J. 116 (2019) 91-98. https://doi.org/10.1016/j.eurpolymj.2019.03.058.

[16] Y. Ren, J. Zhang, J. Gou, F. Chen, F. Yan, Porous poly(ionic liquid) membranes as efficient and recyclable absorbents for heavy metal ions, Macromol. Rapid Commun. 38 (2017) 1700151. https://doi.org/10.1002/marc.201700151.

[17] V. Cannillo, F. Chiellini, P. Fabbri, A. Sola, Production of Bioglass® 45S5 – Polycaprolactone composite scaffolds, Compos. Struc. 92 (2010) 1823-1832. https://doi.org/10.1016/j.compstruct.2010.01.017.

[18] B.Y. Tay, S.X. Zhang, M.H. Myint, F.L. Ng, M. Chandrasekaran, L. K. A. Tan, Processing of polycaprolactone porous structure for scaffold development, J. Mater. Process. Technol. 182 (2007) 117-121. https://doi.org/10.1016/.jmatprotec.2006.07.016.

[19] C-J Liao, C-F Chen, J-H Chen, S-F Chiang, Y-J Lin, K-Y Chang, Fabrication of porous biodegradable polymer scaffolds using a solvent merging/particle leaching method, Biomed. Mater. Res. 15 (2002) 676-681. https://doi.org/ 10.1002/jbm.10030.

[20] L. Oliveira-Salmazo, A. López-Gil, F. Silva-Bellucci, A.E. Job, M.A. Rodríguez-Pérez, Natural rubber foams with anisotropic cellular structures: Mechanical properties and modelling, Ind. Crop. Prod. 80 (2016) 26-35. https://doi.org/10.1016/j.indcrop.2015.10.050.

[21] J.A. Reglero Ruiz, S. Vallejos, Blanca S. Pascual, C. Ramos, S. Beltrán, Félix C. García, José M. García, Microcellular polymer films based on cross-linked 1-vinyl-2-pyrrolidone and methyl methacrylate, J. Supercrit. Fluid. 140 (2018) 270-278. https://doi.org/10.1016/j.supflu.2018.07.011.

[22] S. Siripurapu, R.J. Desimone, S.A. Khan, J.M. Spontak, Low-temperature, surface-mediated foaming of polymer films, Adv. Mater. 16 (2004) 989-994. https://doi.org/10.1002/adma.200306407.

[23] M.T. Kabomo, F.D. Blum, Glass transition behavior of PMMA thin films, Polym. Prep. 42 (2001) 67-68.

[24] C.B. Roth, A. Pound, S.W. Kamp, C.A. Murray, J.R. Dutcher, Molecular-weight dependence of the glass transition temperature of freely-standing poly(methyl methacrylate) films. Eur. Phys. J. E. 20 (2006) 441-448. https://doi.org/10.1140/epje/i2006-10034-0.

[25] K. Geng, O.K.C. Tsui, Effects of polymer tacticity and molecular weight on the glass transition temperature of poly(methyl methacrylate) films on silica, Macromolecules 49 (2016) 2671–2678. https://doi.org/10.1021/acs.macromol.6b00108.

[26] I.M. Smallwood, Handbook of Organic Solvent Properties, first ed., London, 1996.

[27] V. Bellenger, J. Kaltenecker-Commerçon, J. Verdu, P. Tordjeman, Interactions of solvents with poly(methyl methacrylate), Polymer 38 (1997) 4175-4184. https://doi.org/10.1016/S0032-3861(96)01004-X.

[28] A. Marciniak, The solubility parameters of ionic liquids, Int. J. Mol. Sci. 11 (2010) 1973-1990. https://doi.org/10.3390/ijms11051973.

[29] Q. Wang, Y. Chen, L. Deng, Z. Zhang, Determination of the solubility parameter of ionic liquid 1-allyl-3-methylimidazolium chloride by inverse gas chromatography, J. Mol. Liq. 180 (2013) 135-138. http://dx.doi.org/10.1016/j.molliq.2013.01.012.

[30] X. Chen, C. Yuan, C.K.Y. Wing, G. Zhang, Molecular modelling of temperature dependence of solubility parameters for amorphous polymers, J. Mol. Model. 18 (2012) 2333–2341. https://doi.org/10.1007/s00894-011-1249-3.

[31] Z. Ma, G. Zhang, Q. Yang, X. Shi, A. Shi, Fabrication of microcellular polycarbonate foams with unimodal or bimodal cell-size distributions using supercritical carbon dioxide as a blowing agent, J. Cell. Plast. 50 (2014) 55-79. https://doi.org/10.1177/0021955X13503849.

[32] P.D. Condo, I.C. Sánchez, C.G. Panayiotou, K.P. Johnston, Glass transition behavior including retrograde vitrification of polymers with compressed fluid diluents, Macromolecules 25 (1992) 6119-6127. https://doi.org/10.1021/ma00049a007.

[33] Z. Zhang, Y.P. Handa, A new technique for measuring retrograde vitrification in polymer–gas systems and for making ultramicrocellular foams from the retrograde phase, J. Polym. Sci. B, 38 (2000) 716-725. https://doi.org/10.1002/(SICI)1099-0488(20000301)38:5<716::AID-POLB9>3.0.CO;2-N.

[34] P. Alessi, A. Cortesi, I. Kikic, F. Veccione, Plasticization of polymers with supercritical carbon dioxide: Experimental determination of glass-transition temperatures, J. Polym. Sci. 88 (2003) 2189-2193. https://doi.org/10.1002/app.11881.

[35] Y.D. Hwang, S.W. Cha, The relationship between gas absorption and the glass transition temperature in a batch microcellular foaming process, Polym. Test. 21 (2002) 269-275. https://doi.org/10.1016/S0142-9418(01)00081-2.

[36] R. Li, D. Zeng, Q. Liu, L. Li, T. Fang, Physical properties of microcellular polymeric foams with supercritical CO_2, Polym. Plast. Techno. Eng. 54 (2015) 250-256. https://doi.org/10.1179/1432891714Z.0000000001087.

[37] H. Matsuyama, S. Berghmans, D.R Loyd, Formation of hydrophilic microporous membranes via thermally induced phase separation, J. Membrane Sci. 142 (1998) 213-224. https://doi.org/10.1016/S0376-7388(97)00330-X.

[38] Y. Su, C. Chen, Y. Li, J. Li, PVDF membrane formation via thermally induced phase separation, J. Macromol. Sci. A 1 (2007) 99-104. https://doi.org/10.1080/10601320601044575.

[39] I. Tsivintzelis, A.G. Angelopoulou, C. Panayiotou, Foaming of polymers with supercritical CO_2: An experimental and theoretical study, Polymer 48 (2007) 5928-5939. https://doi.org/10.1016/j.polymer.2007.08.004.

[40] G. Wang, J. Zhao, L.H. Mark, G. Wang, K. Yu, C. Wang, C.B. Park, G. Zhao, Ultra-tough and super thermal-insulation nanocellular PMMA/TPU, Chem. Eng. J. 325 (2017) 632-646. https://doi.org/10.1016/j.cej.2017.05.116.

[41] G. Wang, J. Zhao, G. Wang, L.H. Mark, C.B. Park, G. Zhao, Low-density and structure-tunable microcellular PMMA foams with improved thermal-insulation and compressive mechanical properties, Eur. Polym. J. 295 (2017) 382-393. https://doi.org/10.1016/ j.eurpolymj.2017.08.025.

[42] C. Okolieocha, D. Raps, K. Subramaniam, V. Altstädt, Microcellular to nanocellular polymer foams: Progress (2004–2015) and future directions – A review, Eur. Polym. J. 73 (2015) 500-519. https://doi.org/10.1016/j.eurpolymj.2015.11.001.

- An alternative route to obtain microporous PMMA using ionic liquids is presented
- This novel procedure has been compared to classical ScCO$_2$ foaming process
- Microporous morphology is directly controlled by the ionic liquid proportion
- Porous PMMA obtained from ionic liquids present better mechanical properties
- Surface aspect, surface porosity and rugosity is improved using ionic liquids

Declaration of interests

☒ The authors declare that they have no known competing financial interests or personal relationships that could have appeared to influence the work reported in this paper.

☐The authors declare the following financial interests/personal relationships which may be considered as potential competing interests: